

RESEARCH ARTICLE

Cryo-image Analysis of Tumor Cell Migration, Invasion, and Dispersal in a Mouse Xenograft Model of Human Glioblastoma Multiforme

Mohammed Q. Qutaish,¹ Kristin E. Sullivant,¹ Susan M. Burden-Gulley,³ Hong Lu,¹ Debashish Roy,¹ Jing Wang,¹ James P. Babilion,^{1,2,5} Susann M. Brady-Kalnay,^{3,4} David L. Wilson^{1,2,5}

¹Department of Biomedical Engineering, Case Western Reserve University, Room 319 Wickenden Bldg., 2071 Martin Luther King Jr. Drive, Cleveland, OH, 44106-7207, USA

²Department of Radiology, University Hospitals of Cleveland, Cleveland, OH, USA

³Department of Molecular Biology and Microbiology, Case Western Reserve University, Cleveland, OH, USA

⁴Department of Neuroscience, Case Western Reserve University, Cleveland, OH, USA

⁵NFCR Center for Molecular Imaging, Case Western Reserve University, Cleveland, OH, USA

Abstract

Purpose: The goals of this study were to create cryo-imaging methods to quantify characteristics (size, dispersal, and blood vessel density) of mouse orthotopic models of glioblastoma multiforme (GBM) and to enable studies of tumor biology, targeted imaging agents, and theranostic nanoparticles.

Procedures: Green fluorescent protein-labeled, human glioma LN-229 cells were implanted into mouse brain. At 20–38 days, cryo-imaging gave whole brain, 4-GB, 3D microscopic images of bright field anatomy, including vasculature, and fluorescent tumor. Image analysis/visualization methods were developed.

Results: Vessel visualization and segmentation methods successfully enabled analyses. The main tumor mass volume, the number of dispersed clusters, the number of cells/cluster, and the percent dispersed volume all increase with age of the tumor. Histograms of dispersal distance give a mean and median of 63 and 56 μm , respectively, averaged over all brains. Dispersal distance tends to increase with age of the tumors. Dispersal tends to occur along blood vessels. Blood vessel density did not appear to increase in and around the tumor with this cell line.

Conclusion: Cryo-imaging and software allow, for the first time, 3D, whole brain, microscopic characterization of a tumor from a particular cell line. LN-229 exhibits considerable dispersal along blood vessels, a characteristic of human tumors that limits treatment success.

Key words: Glioblastoma multiforme, GBM, Migration, Dispersal, Invasion, Blood vessel detection, 3D region growing, Cryo-imaging, LN-229

Electronic supplementary material The online version of this article (doi:10.1007/s11307-011-0525-z) contains supplementary material, which is available to authorized users.

Correspondence to: David Wilson; e-mail: david.wilson@case.edu

Introduction

Glioblastoma multiforme (GBM) is the most common primary brain neoplasm, with a median patient survival time of 1 year following diagnosis [1]. This poor prognosis

is due in part to uncontrolled proliferation in the restricted cranial space and the highly dispersive nature of the cells [2, 3]. GBM cell dispersal occurs along characteristic pathways of anatomical structures in the brain including the meninges, myelinated fiber tracts, ventricular lining, and perivascular regions [3–5]. Multiple theories exist as to why glioma cells choose these pathways [2]. First, they may be the pathways of least resistance with larger intercellular spaces conducive to glioma cell invasion. In the case of myelinated fiber tracts, fibers are aligned such that cells could migrate along them with reduced barriers. Second, these pathways are rich in cell adhesion molecules and extracellular matrix molecules (ECM) that are permissive substrates for cell migration. Glioma cells have been shown to upregulate integrin receptor expression, thus giving them the ability to interact with ECM molecules found in close association with the brain vasculature [6]. It is important to be able to characterize dispersal in order to determine the effects of cell source, cell markers, and therapeutics, as well as the ability of emerging imaging agents and theranostic nanoparticles to detect/treat dispersed tumor cells. Notably, limited dispersal has been observed to date when injecting human glioma cell lines in a mouse [7, 8].

Our lab developed the Case whole mouse cryo-imaging system, which we believe is uniquely suited for characterization of brain tumor models. Cryo-imaging provides 3D microscopic color bright field anatomy and molecular fluorescence images over vast volumes such as an entire mouse or organ [9–13]. Cryo-imaging consists of a fully automated system for repeated physical sectioning and tiled microscope imaging of a tissue block face, providing anatomical bright field and molecular fluorescence, as well as 3D microscopic imaging. Briefly, the fully automated system alternately sections and acquires tiled color bright field and molecular fluorescence images of the block face of frozen tissue. Components include a whole mouse cryo-microtome, multi-functional microscope imaging system, robotic positioner, and hands-off acquisition software capable of acquiring thousands of tiled images. Image volumes can exceed 200 GB, and specialized workstations and multi-resolution software allow one to visualize a whole mouse on the screen and zoom to ever greater resolution until one can see single fluorescent cells.

In this study of brain tumors, we need to microscopically characterize cell dispersal over the volume of an entire mouse brain, a need uniquely satisfied with cryo-imaging. Volumes of view from confocal and multi-photon microscopy would be $\approx 1/30,000$ the size of the brain, and *in vivo* methods (magnetic resonance imaging (MRI), positron emission tomography (PET), *etc.*) would not image dispersing cells. Potentially, a whole mouse brain could be imaged using histological serial sections, a digital slide scanner, and 3D software. As compared to cryo-imaging, advantages would be even greater resolution and the potential to use histological stains and immunohistology. Disadvantages include the large number of slides required; very time-

consuming manual labor; inaccuracy of registration due to tissue shrinkage, tears, and warping; potential loss of green fluorescent protein (GFP) signal; and added autofluorescence from slide processing. In addition, our long range goal is to image signal from targeted imaging agents and theranostics. Such exogenous signals could be lost in histological processing. In addition, histological sections do not allow one to unequivocally show dispersed cells disconnected from the main tumor mass in 3D. Cryo-imaging also has several advantages over *in vivo* imaging modalities such as MRI and PET. Currently, there is no standard reporter gene technology for MRI. Any cell labeling technique used at implantation would dissipate over the time required to develop a tumor. Additionally, although MRI offers good tumor contrast in the brain with contrast agent, the resolution is insufficient to image single cells dispersing away from the main tumor mass. Although there are now standard reporter gene technologies for PET, it does not have the resolution to detect dispersing cells. We anticipate that cryo-imaging will enable imaging of tumor, dispersed cells, vasculature, and other structures in the brain. The combined features of high resolution, large volume of view, and single cell sensitivity of cryo-imaging make it an ideal imaging modality for the study of tumor cell dispersal.

This study is part of a larger effort at Case Western Reserve University to develop representative animal models of GBM, targeted imaging agents, and targeted therapeutics. In this report, we evaluate the migration and dispersal of the GFP-expressing LN-229 human glioma cell line, following orthotopic injection into mouse brains. The goal is to assess migration (the active process of growth along specific structures in the brain) and dispersal (cells that are physically disconnected from the main tumor) of the fluorescently labeled cells. To achieve this, we find it necessary to create a specialized software to analyze cell migration and dispersal in relation to the vasculature. In the next section, we describe the specialized software developed for this project and experimental methods.

Materials and Methods

Experimental Method and Materials

Orthotopic Xenograft Intracranial Tumors Human LN-229 glioma cells were obtained from the American Type Culture Collection, Manassas, VA, USA. LN-229 cells were infected with lentivirus to express GFP 48 h prior to harvesting [14]. NIH athymic nude female mice (5–8 weeks and 20–25 g upon arrival, NCI-NIH) were maintained at the Athymic Animal Core Facility at Case Western Reserve University according to institutional policies. All animal protocols were IACUC-approved.

LN-229-GFP cells were harvested for intracranial implantation by trypsinization and concentrated to 1×10^5 cells per μl of PBS. For intracranial implants, NIH athymic nude female mice were anesthetized by intraperitoneal injection of 50 mg/kg ketamine/xylazine and fitted into a stereotaxic rodent frame (David Kopf Instruments, Tujunga, CA, USA). A small incision was made just

lateral to midline to expose the bregma suture. A small (0.7 mm) burr hole was drilled at AP=+0.5, ML=-2.0 from bregma. Glioma cells were slowly deposited at a rate of 1 $\mu\text{l}/\text{min}$ in the right striatum at a depth of -2 to -3 mm from dura with a 10- μl syringe (26 G needle; Hamilton Company; Reno, NV, USA); each of the mice was injected with 2×10^5 cells. The needle was slowly withdrawn and the incision was closed with sutures.

After an appropriate period of tumor growth (20–38 days), the animals were sacrificed and the brains were embedded in Tissue-Tek OCT compound (Sakura Finetek U.S.A., Inc. Torrance, CA, USA), rapidly frozen in a dry ice/ethanol slurry, and transferred to the stage of the cryo-imaging device for temperature equilibration.

In addition, we analyzed tissue sections from a brain sample (tumor 6, 25 days post-implantation). The brain was fixed with 4% paraformaldehyde, cryoprotected by incubation in sucrose solutions (10–25%), and then frozen in OCT as above. Tissue sections were cut at 5–7 μm thickness on a Leica cryostat. For immunolabeling of blood vessels, sections were incubated with the endothelial cell-specific antibody CD-31 (B-D Biosciences, catalog number 550274).

Cryo-imaging of Tissue Samples

Using techniques in this report, we have cryo-imaged and analyzed over 14 mouse brain tumors. Here we focus on the results from five brains at 20, 28, 29, 36, and 38 days post-implantation. In some instances, we perfused the mouse with India ink as a contrast agent for blood vessels. Frozen brains were sectioned and imaged using the cryo-imaging system at two different in-plane resolutions and section thicknesses: $11 \times 11 \mu\text{m}$ pixels and 15 μm section thickness and $15.6 \times 15.6 \mu\text{m}$ pixels and 40 μm section thickness. When imaging at resolutions of 15.6×15.6 and $11 \times 11 \mu\text{m}$, the fields of view were 21.22×16.16 and 14.96×11.40 mm, respectively. At each of these resolutions, the brain fit within a single field of view and did not require image tiling. Image acquisition took approximately 3 h when sectioning with 40 μm slice thickness and approximately 5 h when sectioning with 15 μm slice thickness. Bright field and fluorescence images were acquired for each of the brains. Color bright field images were acquired using a liquid crystal RGB filter and a monochrome camera (Retiga EXi, QImaging Inc., Canada). Fluorescence images were acquired using GFP fluorescence filters (Exciter: HQ470/40x, Dichroic: Q495LP, Emitter: HQ500LP, Chroma, Rockingham, VT, USA), a fluorescent light source (XCite 120PC, EXFO, Canada), and the same low light digital camera. Volumes were obtained in a hands-off, automated fashion on our cryo-imaging system [11, 13].

Image Processing Algorithms

We used MATLAB to perform 2D post-processing prior to 3D visualization using Amira. Each raw image was approximately 4 MB. Depending upon slice thickness and brain orientation in the field of view, we acquired from 200 to 450 slices, giving 1.5 to 3.6 GB of raw image data, respectively.

Blood Vessel Visualization

To enable rapid evaluation of perivascular migration and dispersal of glioma cells along blood vessels, we developed specialized

methods for blood vessel visualization using bright field cryo-image data. Blood- or ink-filled vessels are darker than the surrounding brain tissue. To enhance contrast of blood vessel segments, we utilized filters matched to small vessel segments. Since the in-plane pixel spacing (as small as 11 μm) was smaller than the distance between slices (15 or 40 μm), we performed 2D filtering on each slice to enhance vessel contrast relative to background. We used the green channel from color bright field images because this gave higher contrast than other channels. A functional diagram (Fig. 1a) shows the algorithm. The main steps are described below.

Noise Reduction To reduce noise while preserving edges, we employed a modified Wiener filter that adaptively removes the noise based on the statistics of a local region around each pixel in the image [16]. Filter equations are shown in Eqs. 1a–c:

$$\mu = \frac{1}{MN} \sum_{n_1, n_2 \in \gamma} I(n_1, n_2) \quad (1a)$$

$$\sigma^2 = \frac{1}{MN} \sum_{n_1, n_2 \in \gamma} I^2(n_1, n_2) - \mu^2 \quad (1b)$$

$$I_{\text{out}}(n_1, n_2) = \mu + \frac{\sigma^2 + v^2}{\sigma^2} (I(n_1, n_2) - \mu) \quad (1c)$$

where:

(n_1, n_2)	Pixel location in the image
μ	Estimated local mean around a pixel
σ^2	Estimated local variance around a pixel
v^2	The noise variance estimated as the average of all local estimated variances for each pixel in the kernel
γ	The local neighborhood window around each pixel
MN	The size of the window used in filtering

This adaptive filter estimates the local mean and the variance for each pixel in a neighborhood of size MN and uses this estimate to reduce the noise.

Background Removal To increase the contrast of the blood vessels against the surrounding tissue background, we employed unsharp mask processing. We used an arithmetic mean filter to estimate the background in each of the 2D images. The size of the kernel was much larger than the blood vessels and therefore retained them in the output image.

Vessel Edge Detection To detect vessel edges, we used a set of four oriented kernels, known as difference of offset Gaussian filters (DoOG filters) to measure the local gradient in the image [17, 18]. For example, in order to measure the local gradient along the x -direction in the image, the appropriate DoOG kernel is constructed by taking the difference of two copies of Gaussian kernels displaced along the x -axis. For kernel construction, there are three parameters to optimize for vessel enhancement: the standard deviation of the Gaussians, the

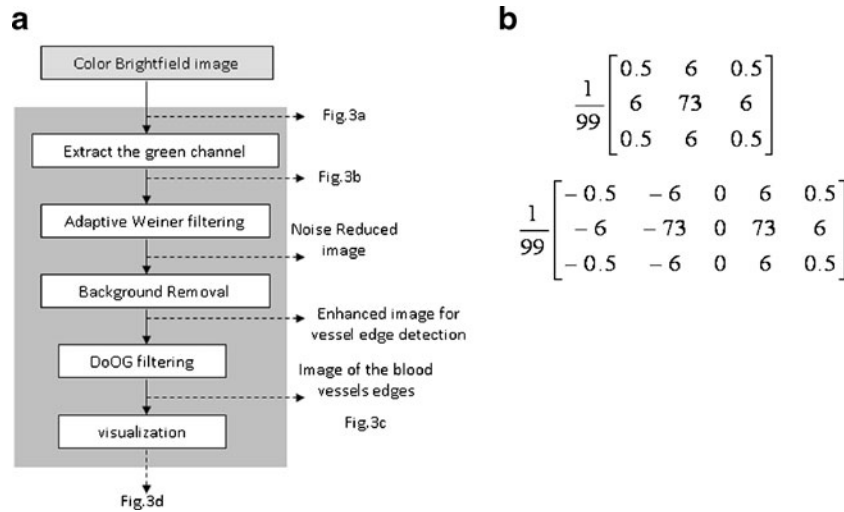


Fig. 1. Blood vessel visualization using bright field images. **a** Functional diagram showing the steps to visualize blood vessels. **b** The particular 2D Gaussian ($\sigma=0.5$) used to construct DoOG kernel (*bottom*) that enhances blood vessels in the x -direction.

truncation size, and the offset between the centers of the Gaussian kernels. The first parameter determines the intensity of the kernel response at the blood vessel edge and the pixels adjacent to the edge. The second parameter determines the thickness of the edge; larger Gaussians will result in a response for adjacent pixels further away from the edge pixels. The last parameter determines the slope of the filter around the zero crossing point of the kernel. To find the best parameters for vessel enhancement, we kept the offset parameter proportional to the standard deviation parameter; specifically, we used $\text{offset} = 4\sigma$ [18]. Then, we experimented to find the best σ and truncation size. Figure 1b shows the particular kernel used to enhance the edges with a maximum response in the x -direction. The other kernels used to enhance the edges in the y -direction and in $(45^\circ, 135^\circ)$ directions are just a rotated version of the kernel shown. We processed the 2D background subtracted images using each of the four kernels. Then we took the absolute value of each of the resultant images to account for both dark/light and light/dark edges. Since the pixels at a particular processed edge will have maximum response resulting from processing that edge by the kernel that best matches that direction, we kept the maximum response for each pixel among the four to form the final image.

Visualization Previous steps gave a gray scale volume with local maxima at edges of blood vessels. To visualize blood vessels in 3D, we created a colored volume that contains the result of the edge enhancement step as the red channel and zero for the green and blue channels. We then performed volume rendering on this colored volume such that the voxel is fully opaque if its red channel value is above a threshold and transparent otherwise. The threshold value is determined interactively during the visualization process. Thresholding removes artifactual noise voxels that are unlikely to be vessel edges. We rendered brain image volumes from 1.5 to 3.6 GB in Amira on a workstation configured with 32 GB of RAM and a video card with 2–4 GB RAM.

Image Segmentation and Visualization of Fluorescent Tumor Cells

We developed a semi-automated method for segmenting the main tumor mass and dispersed cells in a fluorescent cryo-image volume. A functional diagram is shown in Fig. 2. The principal steps are outlined below.

Segmentation of Main Tumor Mass To segment the main tumor mass, we used a 3D seeded region growing algorithm developed in our laboratory which works within the Amira platform. The region grows from the seeded region by including 26-connected voxels which have intensity and gradient magnitude values within preset high/low constraints. To calculate the gradient magnitude, we used a 3D gradient operator where the magnitude of the gradient, g , can be estimated numerically using the central difference operator at location (x, y, z) as given below in Eq. 2, where \max identifies the maximum gradient magnitude in the processed volume.

$$g(x, y, z) = 255 \left(\frac{|\nabla I(x, y, z)|}{|\nabla I(x, y, z)|_{\max}} \right) \quad (2)$$

where:

$$|\nabla I(x, y, z)| = \sqrt{I_x^2 + I_y^2 + I_z^2}$$

$$I_x = I(x-1, y, z) - I(x+1, y, z)$$

$$I_y = I(x, y-1, z) - I(x, y+1, z)$$

$$I_z = I(x, y, z-1) - I(x, y, z+1)$$

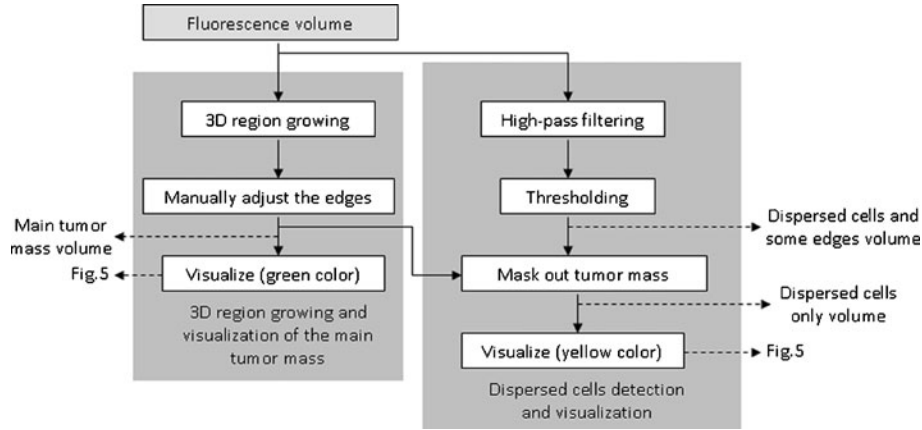


Fig. 2. Tumor visualization using fluorescence images. Functional diagram showing the steps to visualize the main tumor mass and dispersed tumor cells.

Following 3D region growth, each 2D image was reviewed and manually edited if necessary. The main tumor mass volume is visualized in later steps using a green color.

Evaluation of Image Analysis Algorithms In some instances, we compared manual *versus* algorithm-based segmentation. Results were compared using the Dice similarity measure, which is widely accepted as a measure of agreement between segmented regions segmented by two methods [15]. Briefly, the Dice score is given by Eq. 3 below

$$\text{Dice Similarity Coefficient} = \frac{2(\text{segmentation A} \cap \text{segmentation B})}{|\text{segmentation A}| + |\text{segmentation B}|} \quad (3)$$

A Dice score of 0 means there is no overlap between the two segmentations. A score of 1 indicates perfect overlap. Typically, a Dice score >0.700 is deemed acceptable [15].

Dispersed Tumor Cell Detection To detect dispersing single and clustered cells, we created a filter for enhancing fluorescent single tumor cells and clusters. We employed a high-pass filter, which attenuates the low-frequency background signal without disturbing the high-frequency content. Since Gaussian-based filters are common with the advantages of smooth filtering and the lack of ringing, we employed a zero-phase shift high-pass Gaussian filter with the following transfer function shown in Eq. 4 [16]:

$$H(u, v) = 1 - e^{-D^2(u, v)/2\sigma^2} \quad (4)$$

$$D^2(u, v) = \sqrt{\left(u - \frac{M}{2}\right)^2 + \left(v - \frac{N}{2}\right)^2}$$

Where:

$D^2(u, v)$ The distance from the origin of the Fourier transform of the image

$M \times N$ size of the image

σ Standard deviation of the Gaussian

Each of the fluorescence images was converted to frequency domain using the FFT algorithm, filtered using the high-pass Gaussian filter, and converted back to the spatial domain. We thresholded the result of the high-pass filtering then masked out the main tumor mass to create a binary volume of dispersing tumor cells and clusters.

Visualization To easily visualize both dispersed cells and the main tumor mass, we rendered these objects in different pseudo-colors. The main tumor mass was surface-rendered in green. Dispersed tumor cells were volume-rendered in yellow. Blood vessels were rendered in red as described previously. Results were fused to show tumor cell migration and dispersal along blood vessels.

3D Migration Distance of Dispersed Tumor Cells

To analyze dispersal, we measured the 3D distance from the main tumor mass using a morphological distance algorithm. Inputs are binary volumes containing the main tumor mass and dispersed cells, respectively. We resampled the volumes to account for disparities in section thickness and resolution to result in isotropic data. For example, we resampled volumes acquired at $11 \times 11 \times 15$ to $11 \times 11 \times 11 \mu\text{m}$, a size comparable to the size of a tumor cell. To measure distance, we applied a sequence of dilations on the volume containing the main tumor mass using a sphere of increasing diameter as a structuring element. After each dilation, the volume containing the dispersed tumor cells was checked to see if any of the cell-containing voxels were overlapped by the dilation. The steps of the algorithm are:

1. Read binary volumes containing the main tumor mass and dispersed cells, respectively. Sample both volumes to give isotropic voxels and threshold to create binary volumes.
2. In the volume containing dispersed tumor cells, save all the indices of the voxels with non-zero value.
3. Perform 3D dilation on the volume containing the main tumor mass with a sphere structuring element of radius i , starting with $i=1$.

4. If saved indices from step 3 are included in the new dilated volume, record a distance as $i \times 11$ or $i \times 15.6 \mu\text{m}$ and eliminate it from further consideration.
5. Increase the radius of the sphere structuring element i by 1 and go back to step 4. The loop continues until all indices are eliminated.

Histograms of distances and statistical measures (mean, median, etc.) are determined.

Processing speed is an issue because of our large data sets. Processing times of Matlab codes can be reduced by converting to C++. Alternatively, many of our algorithms use image filtering, which is easily accelerated using GPU processing as has recently been done by us for another application [19].

Results

Using our image processing algorithms, we characterized an orthotopic brain tumor model consisting of human LN-229 glioma cells expressing GFP (LN-229-GFP). Images presented here are from three brains, but quantitative dispersal distances were from five LN-229-GFP brains.

We performed experiments to optimize algorithms for vessel edge enhancement and tumor mass segmentation. Using representative bright field and fluorescence images, we processed images and reviewed images in 2D and 3D to optimize visual and quantitative analysis. A 5×5 window size for the Weiner filter and a 15×15 mean filter for unsharp mask processing removed background variations due to anatomy of brain, reduced noise, and preserved large and small vessels. For vessel enhancement with DoOG, optimal results were obtained with 3×3 Gaussian kernels and $\sigma=0.5$ which gives an offset value of 2 pixels between the centers of the Gaussians. These optimized parameters gave a strong response at vessel edges with acceptable noise enhancement. Figure 1b shows the particular kernel used for edge enhancement along the x -direction.

When segmenting the main tumor mass in fluorescence images with the 3D region growth algorithm (Fig. 2), we found that the gradient constraint was more important than the intensity constraint because of overlapping intensity values; this is consistent with bright edges of the main tumor mass. In most cases, a gradient magnitude of 70 stopped region growing at the correct edge. In about 15–20% on an average of 400 total image slices, we manually edited at least a small portion of the segmentation. With this semi-automated solution, we reduced analysis time from 10 h for full manual segmentation to less than 2 h on our large data sets.

We compared segmentations using our semi-automated approach to independent manual segmentations from experienced analysts using the Dice similarity measure (Eq. 3). Analysis was done on a representative 40-slice slab imaged at high resolution, and the algorithm-based analysis was done months apart from manual segmentation. There was excellent agreement between the manual segmentations. Over the three potential pairings, the average Dice score

was 0.88 ± 0.08 , a value much better than 0.7 typically deemed acceptable [15]. Comparing the algorithm-based results to each of the three manual segmentations gave an excellent average Dice score of 0.90 ± 0.08 . We infer that the algorithm-based method was as good as full manual analysis.

The frequency domain, “high-pass” Gaussian filter (Eq. 4) gave visually optimal results with $\sigma=33$ for an image size of $1,036 \times 1,360$ pixels. This value used over all brains completely removed background and retained only dispersed tumor cells and clusters, after thresholding and masking out the main tumor mass.

We compared the number of detected clusters using our automated method to independent manual detection performed by three observers. We accepted a cluster if two of three analysts marked it as a cluster. Manual analysis over a slab of 30 slices resulted in 142 clusters while our algorithm detected 140 clusters. To further compare results, we calculated 3D Euclidian distance between the center of mass of clusters detected by our automated method and clusters detected by manual analysis. We considered clusters identical if the distance between centers of clusters was < 2 voxels. There were 128 common clusters. Tallying results for the algorithm, we have 128 true positives, 12 false positives, and 14 false negatives. The algorithm-based method compared very favorably to manual detection with sensitivity and precision equal to 90.1% and 91.4%, respectively. Accuracy is not computed because the number of true negatives (TNs) can be misleading when TNs consist of the large number of pixels not containing a cluster.

Even without contrast injection, cryo-imaging allows one to visualize blood vessels (Fig. 3). The 2D color bright field images (Fig. 3a) and the corresponding green channel images (Fig. 3b) show dark blood vessels. Detailed brain anatomy such as blood vessels and white matter tract is also evident. After applying the DoOG filter, vessel edges are shown (Fig. 3c), and we have determined that the vessels with diameters $\geq 30 \mu\text{m}$ are clearly visualized with $11 \times 11 \times 15 \mu\text{m}$ imaging resolution. Finally, volume rendering enables 3D visualization of all major blood vessels (Fig. 3d and Movie 1).

Application of the image processing steps for visualization of the tumor and dispersing cells is demonstrated in Fig. 4. In the 2D images from all brains, we observed a very bright main tumor and disconnected small tumor cell clusters (Fig. 4). The tumor is shown in Fig. 4b at the same size as the bright field image in Fig. 4a. In Fig. 4c, d, we show magnified versions of the unprocessed and deconvolved fluorescence images, respectively. We utilized a previously described deconvolution algorithm to confirm that tumor cell clusters were distinct from the main tumor mass [10]. Following deconvolution, scattered light was reduced and we more clearly discerned cell clusters not connected to the main tumor mass. Although scatter deconvolution helped make this determination, it was unnecessary to deconvolve all image data. The high-pass Gaussian filter gave nearly

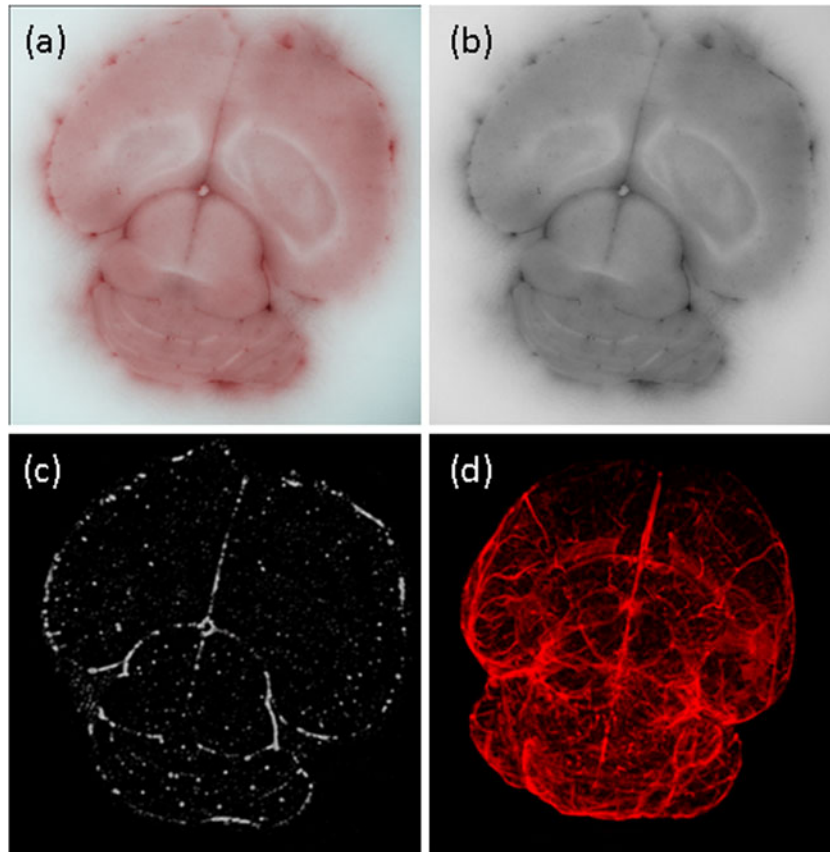


Fig. 3. Steps for blood vessel visualization for tumor 1. **a** The raw color bright field block face image of a brain is shown. **b** Extracted green channel from the image shown in **a** used for further processing. **c** Application of the DoOG filters resulting in a high contrast, 2D image of blood vessel profiles. **d** 3D visualization of the image stack from this brain specimen, showing the detected vasculature of the brain (tumor 1, 20 days post-implantation).

identical results. It removed background signal and enabled reliable detection of dispersed cell clusters. Moreover, deconvolution of our extremely large volumes would have required very excessive processing times, while the filtering operation was quick. Often, the tumor was also visible in bright field images as a light structure (arrow in Fig. 4a).

LN-229 clearly shows migrating dispersed cells (Figs. 5 and 6). As described above, the GFP-labeled main tumor mass was segmented in 3D with a semi-automated region growing algorithm. Disconnected cell clusters were also detected and segmented. In Fig. 5, we show the two tissue types fused together. Higher magnification views of Fig. 5a

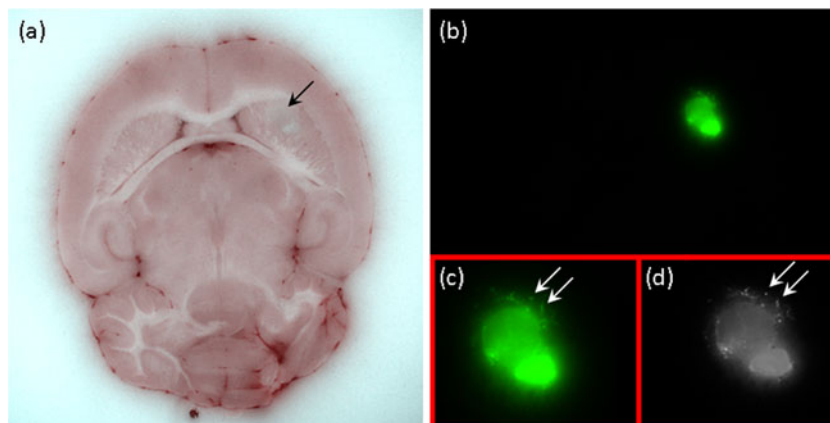


Fig. 4. Steps for visualization of tumor and dispersing cells for tumor 2. **a** The raw color bright field block face image of a brain is shown. *Arrow* indicates approximate position of the LN-229-GFP tumor within this section. **b** Corresponding fluorescence image showing the LN-229-GFP tumor (*green*). **c** Higher magnification view of the main tumor shown in **b** with cells dispersing away from the tumor edge (*arrows*). **d** Deconvolved fluorescence image shown in **c** (tumor 2, 36 days post-implantation).

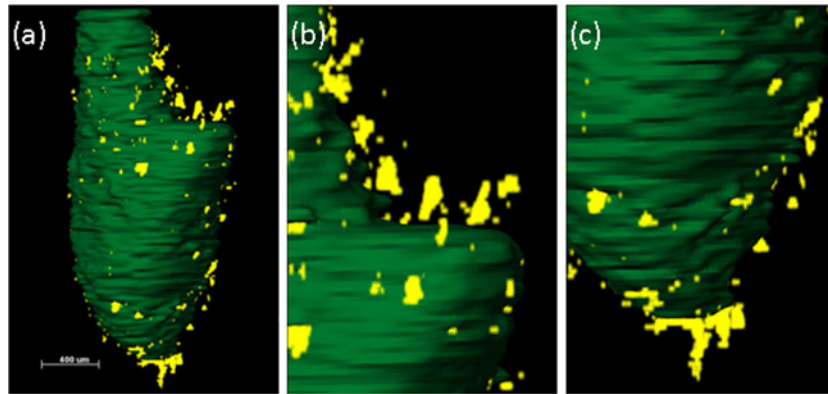


Fig. 5. Results of the dispersed cell detection algorithm for tumor 1. **a** 3D rendering of both the main tumor (*green*) and the dispersed cells (*yellow*). **b, c** Higher magnification views of dispersed cells shown in **a** (tumor 1, 20 days post-implantation).

are shown in panels **b** and **c** of Fig. 5 to illustrate that clusters are clearly disconnected from the main tumor mass. Accuracy was confirmed through visual inspection of processed images compared with the original raw data. Standard histological sections of a LN-229-GFP tumor also show cell dispersal from the tumor (Fig. 6a, b). Dispersed cells are often in close proximity to blood vessels (Fig. 6c, d). From these 2D images, one cannot determine whether cells are truly disconnected from the main tumor mass or are a continuous projection. The 3D images from cryo-imaging provide a more complete view of tumor architecture and cell dispersal.

Growth of the main tumor mass often follows blood vessels (Fig. 7). In 2D, we see that the fluorescent tumor (Fig. 7b) follows along the vessel identified in bright field in Fig. 7a. In Fig. 7c, the segmented $\approx 50\text{-}\mu\text{m}$ diameter vessel is superimposed on the fluorescent tumor. Migration is more appropriately visualized in 3D (Fig. 7d); one can clearly see the green tumor projection growing along the blood vessel. This substantial tumor projection accounts for about 5% of the tumor mass.

We further examined tumor cell migration leading to dispersal of unattached tumor clusters along blood vessels. In Fig. 8, we fuse the main tumor mass (*green*), dispersed

tumor cells (*yellow*), and blood vessels (*red*) at different magnifications and orientations. In this brain only 20 days after implantation, tumor volume was 1.78 mm^3 , and the number of dispersed clusters was 761, representing $\approx 1.17\%$ of the main tumor volume (see Movie 2). Arrows in Fig. 8c point to examples of tumor cell clusters dispersed along blood vessels. Assuming a cell volume of ≈ 1 voxel ($11 \times 11 \times 15\ \mu\text{m}$) and running a connected components analysis on the clusters, fluorescent clusters along blood vessels ranged from single cells to small clusters of up to ten cells.

We characterized cell dispersal as a function of time post-implantation. With increasing time post-implantation (20–38 days), there was increased tumor volume, dispersed cell volume, number of clusters, and number of voxels per cluster. We found a marked increase of large dispersed clusters for tumors with time post-implantation. For example, comparing 20 and 38 days post-implantation, we found a small percentage of the number of clusters (2.2%) having a size ≥ 5 voxels/cluster at 20 days post-implantation, as compared to 49.4% at 38 days post-implantation. We also found sporadic instances exclusive to tumors with longer times post-implantation of clusters $>1,000$ voxels/cluster. Over the course of 20–38 days post-implantation, main

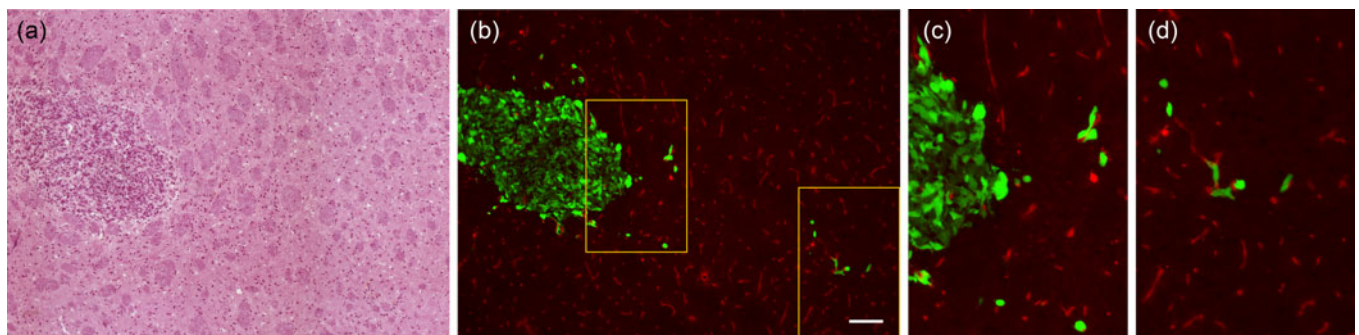


Fig. 6. LN-229 tumor cell dispersal in 2D. **b–d** Histological section of a GFP-expressing tumor xenograft of LN-229 cells (*green* fluorescence) was immunolabeled with the endothelial cell specific antibody CD-31 and visualized with a secondary antibody conjugated to Texas Red. **a** Bright field image from the same section stained with hematoxylin and eosin is shown. **b** Dispersing cells were observed at varying distances from the main tumor mass, as indicated by expression of GFP. **c, d** Higher magnification views of the *boxed regions* in **b** indicate a close association of dispersing cells with blood vessels. Scale bar represents $100\ \mu\text{m}$ (tumor 6, 25 days post-implantation).

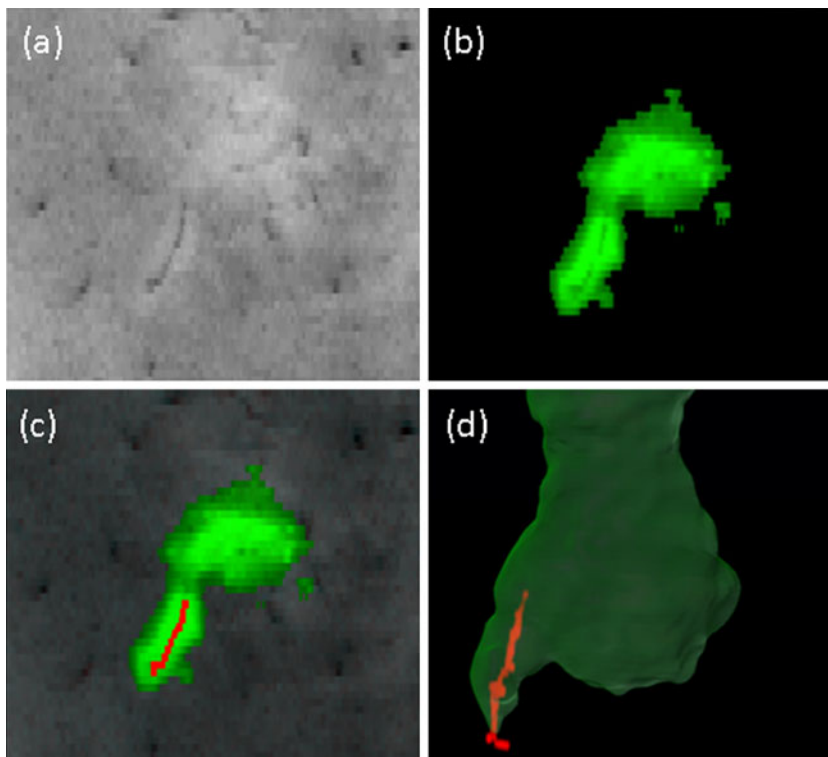


Fig. 7. Projection of tumor growth along a blood vessel shown for tumor 5. **a** Dark blood vessels are shown in the color bright field image following perfusion with India ink. **b** The corresponding 2D fluorescence image clearly shows GFP-labeled tumor. **c** The vessel is segmented and a 2D fusion shows the projection of cells growing along the vessel. **d** A 3D visualization clearly shows a substantive ($\approx 5\%$ of total tumor volume) projection of the green tumor growing along the blood vessel (*red*) (tumor 5, 38 days post-implantation).

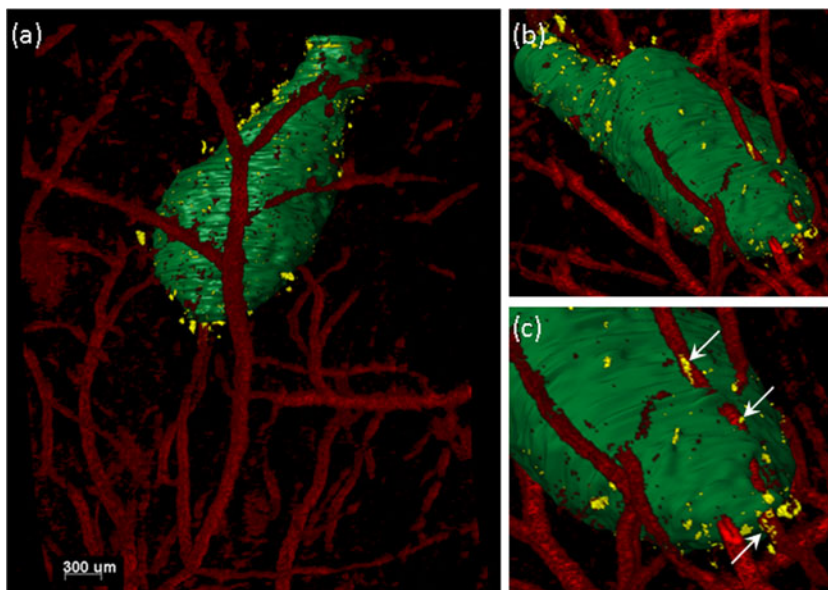


Fig. 8. Tumor cells dispersing along blood vessels shown for tumor 1. In **a**, cryo-images from a mouse brain containing a LN-229-GFP tumor were processed using the algorithms for visualization of main tumor mass (*green*), tumor cell dispersal (*yellow*), and blood vessel visualization (*red*). **b** Higher magnification image of tumor and surrounding vasculature viewed from a different angle. **c** Higher magnification image of small tumor cell clusters dispersing along blood vessels (*arrows*) (tumor 1, 20 days post-implantation).

tumor volume increased from 1.78 to 2.09 mm³, and the volume of dispersed cells increased from 0.021 to 0.119 mm³ giving dispersed cell volumes of 1.17% and 5.71% of the main tumor mass for days 20 and 38, respectively. Also, the number of dispersed clusters increased from 761 to 3,605, the average number of voxels per cluster increased from 1.6 to 42.6 voxels/cluster, and the median number increased from 1 to 6 voxels/cluster. If we assume the voxel size is approximately equivalent to a cell, we can estimate the number of cells per cluster from the above results.

We measured dispersal distances (Fig. 9). Plotted are histograms of distances, normalized as percentages. We show the results of tumors at 20 and 38 days post-implantation. Other brains showed similar patterns of tumor cell migration and dispersal. Although most tumor cells were within 70 μ m, some had dispersed >100 μ m from the main tumor. The mean and median values of dispersal distance for all analyzed brains are 63 and 53 μ m, respectively. Also, at later time points (36–38 days post-implantation), we noticed dispersal distances increased to >200 μ m from the main tumor, a distance that represents \approx 2.5% of the brain diameter. Both mean and median of dispersal distance tended to increase with time post-implantation.

Finally, there was no evidence of blood vessel density increase in and around the LN-229 tumor. We analyzed a region of interest (ROI) around the tumor and compared that to the same ROI placed in a comparable position on the contralateral side of the same brain. Both visual inspection and quantitative analysis indicated no significant difference in density for vessels \geq 30 μ m. Quantitative assessment was done by counting blood vessel voxels. The results showed a slight increase in blood vessels \approx 5%. However, this small increase may be partly due to error in the measurement method used for this analysis. Therefore, the measured difference in blood vessels is not enough evidence of significant angiogenesis in LN-229 tumors over the course of 38 days post-implantation.

Discussion

The ability to characterize migration and dispersal of glioma tumor cells in orthotopic tumor models is highly significant. The efficacy of chemotherapeutic agents lies in their ability to block proliferation, survival, migration, dispersal, invasion, and/or metastasis of tumor cells. Since metastases are typically not seen in human glioma, tumor cell migration and dispersal are the “spreading” mechanisms of interest. To be useful, an orthotopic xenograft animal model of human glioma cell lines should display patterns of tumor cell migration and dispersal characteristic of human GBM tumors. An appropriate animal model will have a large impact on gene and biologic drug therapeutics discovery, as well as improvements in imaging brain tumors. We have great interest in imaging cell dispersal from brain tumors in these models to assess the ability to mark dispersing tumor cells with molecular imaging probes. Ultimately, we want to determine if such imaging probes can be used to enhance surgical resection and to improve survival of patients.

Cryo-imaging and software allow, for the first time, 3D analysis of migration and dispersal of cells throughout an entire brain. The Case cryo-imaging system is well suited for this task because it provides 3D microscopic resolution, color anatomy, and molecular fluorescence images of large tissue specimens. In addition to fluorescence imaging of tumor cells, bright field images can be used to visualize blood vessels, white matter tracts, *etc.* There is no good single cell sensitivity, whole organ imaging alternative. For example, the size of a typical confocal image stack (170 \times 170 \times 500 μ m) is only 1/30,000 of the volume of a mouse brain. Another alternative is the use of 2D histology sections. Manual labor is significant, sampling errors can occur, and it is impossible to determine if cells are disconnected from the main tumor mass in 2D. One can obtain serial histology sections and create a 3D image volume in software. However, such methods are fraught with problems. Sections can shrink, tear, and otherwise distort the image, confounding accurate 3D alignment.

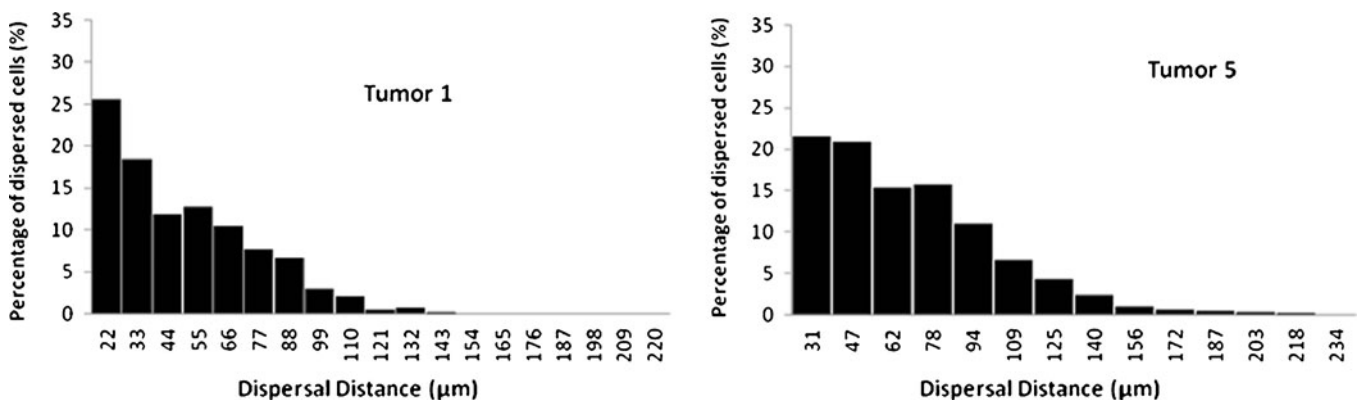


Fig. 9. Dispersal distances from the main tumor mass. Histograms are shown with the number of cells normalized as a percentage. Specimens are analyzed at 20 (a) and 38 (b) days post-implantation. Clearly most dispersed cells are within 70 μ m. Longer distances are recorded with increasing time post-implantation. Other tumors show a similar pattern of dispersal. Total number of dispersed clusters in these brains is 761 and 3,605 for tumors 1 and 5, respectively.

Consequently, *in vivo* modalities (MRI, PET, *etc.*) can benefit from cryo-imaging by validating the 3D results with the single cell resolution of cryo-images rather than with histology or confocal imaging.

We now discuss the first of three important algorithms to aid characterization of migration and dispersal of glioma cells, particularly along blood vessels. To visualize blood vessels in bright field cryo-image volumes, we use filters optimized to reduce noise and enhance vessels in volume visualizations. The Wiener filter reduces noise while retaining edges and the DoOG filters effectively enhance vessel edges. DoOG suppresses noise and enhances vessel edges much better than simpler filters (*e.g.*, Sobel) and computes faster on our very large data sets than more complex alternatives (*e.g.*, level set-based algorithms). Visual inspection of results and comparison to raw images prove that this approach enhances most of the larger vessels in the brain. Detection of smaller vessels is limited by image resolution since contrast of smaller vessels against brain tissue diminishes at lower resolution due to the partial volume effect. With an in-plane resolution of 11 μm , we are able to detect decidedly more vessels as compared to data sets with 15.6 μm in-plane resolution. Similarly, with thinner sections, blood vessel continuity is improved. With 3D rendering of high-resolution brains, one can reliably visualize vessels with diameters as small as 30 μm . Because this is a filtering technique, processing is relatively fast (≈ 90 min) even on extremely large (2 GB) data volumes. Results are robust with little sensitivity to processing parameters. Processing allows visualization of blood vessels from the color of accumulated blood. No contrast agent is needed. This should be quite advantageous for assessing targeted imaging agents and nanoparticle theranostics because no potentially disruptive perfusion agent must be applied.

The second algorithm separately segments the tumor mass and dispersed cells. The 3D region growing method includes both intensity and low edge strength inclusion criteria. In practice, the low edge strength criterion is most important for getting accurate results. Nevertheless, we had to manually adjust at least a small portion of the boundary in about 20% of cases, or typically 100 out of 500 image slices. By implementing our region growing algorithm within Amira, we have access to very useful editing tools, including interactive editing in 3D. Typically, editing takes 2 h as compared to 10 h for a full manual segmentation. As determined from Dice scoring, the algorithm-based method compared very favorably to independent manual segmentations. As a result, we infer that an algorithm-based segmentation is as good as a full manual analysis. High-pass Gaussian filtering allowed us to detect the dispersing cells with a simple interactive threshold. Rendering the two volumes in different colors makes the dispersed cells/clusters easy to distinguish from the main tumor.

Visual inspection of rendered 3D volumes clearly shows spaces between the yellow dispersing tumor cell clusters and the main tumor mass. Fusing results with the blood vessel

volume illustrates the migration and dispersal of the tumor cells along blood vessels. In some instances, we used 3D stereo display (NVIDIA 3D stereo) to quickly assess these spatial relationships. Our algorithms showed improved results for the higher resolution brain as compared to the lower resolution brains. At high resolution, we were able to detect and visualize vessels as small as 30 μm and assess the tumor cell migration and dispersal distance more accurately. Although a subset of tumor cell clusters dispersed along blood vessels, other clusters dispersed without following blood vessels. By analyzing the 2D images, we noticed that such clusters were either dispersing along the white matter tract, which is one of the characteristic pathways for dispersal, or these clusters were around very small blood vessels that we were not able to detect due to the very low contrast between such vessels and the brain tissue. There is a marked increase in the number of cells/cluster with time post-implantation, indicating that the dispersed clusters are growing. Many of the larger clusters are found along blood vessels that we detected (≥ 30 μm diameter).

The third algorithm measures tumor cell dispersal distance away from the main tumor mass in 3D. In our study, we determined that tumors at later times post-implantation showed a slight increase in dispersal distance and a larger increase in dispersed cell volume. Dispersal distances from 2D histology sections were comparable to those seen with cryo-imaging. However, with 2D sections, one has no way of knowing if cells are connected to the tumor mass in 3D, and one painstakingly makes 2D measurements made more appropriately in 3D. Dispersal distance histograms and statistical measures provide an understanding of the aggressive nature of the LN-229 cell line. We believe that the algorithm will provide a fast, accurate method for comparing cell dispersal among different cell lines, time post-implantation, the mouse host environment, and treatments.

Conclusions

Cryo-imaging and software allow, for the first time, 3D, whole brain, microscopic characterization of a glioblastoma multiforme tumor model. Not only did we visualize cell migration and dispersal, but also we quantitatively assessed dispersal distance of tumor cell clusters from the main tumor mass. Furthermore, dispersal along blood vessels was clearly identified. Cryo-imaging uniquely allows us to easily image the entire brain and detect even single dispersing fluorescent cells. It is impossible to make such characterizations with traditional *in vivo* imaging (MRI, PET, *etc.*) or with histological sections. This study can be extended to characterize the migration, invasion, dispersal, and metastasis in other tumor types and to characterize imaging agents and therapeutic effects.

Acknowledgments. The authors would like to acknowledge the expert technical help of Miss Catherine Doller and Dr. Scott Howell with tissue

histology. This work was supported by the Case Center for Imaging Research. The research was also supported by grants Ohio Wright Center/BRTT, The Biomedical Structure, Functional and Molecular Imaging Enterprise (D.L.W.), National Institutes of Health grants R42CA124270 (D.L.W.), T32EB007509 (K.E.S), R01-NS051520 (S.B.-K.), and R01-NS063971 (S.B.-K., D.L.W. and J.P.B.).

Conflict of Interest. Debashish Roy, David L. Wilson, Mohammed Q. Qutaish, and Kristin E. Sullivant are inventors of cryo-imaging technology licensed by CWRU. Debashish Roy and David L. Wilson are officers with ownership positions at BioInVision, Inc., which is commercializing cryo-imaging.

References

1. Jacob G, Dinca EB (2009) Current data and strategy in glioblastoma multiforme. *J Med Life* 2:386–393
2. Furnari FB, Fenton T, Bachoo RM, Mukasa A, Stommel JM, Stegh A, Hahn WC, Ligon KL, Louis DN, Brennan C, Chin L, DePinho RA, Cavenee WK (2007) Malignant astrocytic glioma: genetics, biology, and paths to treatment. *Genes Dev* 21:2683–2710
3. Ichimura K, Ohgaki H, Kleihues P, Collins VP (2004) Molecular pathogenesis of astrocytic tumours. *J Neurooncol* 70:137–160
4. Louis DN, Ohgaki H, Wiestler OD, Cavenee WK, Burger PC, Jouvet A, Scheithauer BW, Kleihues P (2007) The 2007 WHO classification of tumours of the central nervous system. *Acta Neuropathol* 114:97–109
5. Louis DN (2006) Molecular pathology of malignant gliomas. *Annu Rev Pathol* 1:97–117
6. Teodorczyk M, Martin-Villalba A (2010) Sensing invasion: cell surface receptors driving spreading of glioblastoma. *J Cell Physiol* 222:1–10
7. Candolfi M, Curtin JF, Nichols WS, Muhammad AG, King GD, Pluhar GE, McNeil EA, Ohlfest JR, Freese AB, Moore PF, Lerner J, Lowenstein PR, Castro MG (2007) Intracranial glioblastoma models in preclinical neuro-oncology: neuropathological characterization and tumor progression. *J Neurooncol* 85:133–148
8. Barth RF, Kaur B (2009) Rat brain tumor models in experimental neuro-oncology: the C6, 9L, T9, RG2, F98, BT4C, RT-2 and CNS-1 gliomas. *J Neurooncol* 94:299–312
9. Gargsha M, Qutaish MQ, Roy D, Steyer GJ, Watanabe M, Wilson DL (2011) Visualization of color anatomy and molecular fluorescence in whole-mouse cryo-imaging. *Comput Med Imaging Graph* 35:195–205
10. Krishnamurthi G, Wang CY, Steyer G, Wilson DL (2010) Removal of subsurface fluorescence in cryo-imaging using deconvolution. *Opt Express* 18:22324–22338
11. Roy D, Steyer GJ, Gargsha M, Stone ME, Wilson DL (2009) 3D cryo-imaging: a very high-resolution view of the whole mouse. *Anat Rec (Hoboken)* 292:342–351
12. Steyer GJ, Roy D, Salvado O, Stone ME, Wilson DL (2009) Removal of out-of-plane fluorescence for single cell visualization and quantification in cryo-imaging. *Ann Biomed Eng* 37:1613–1628
13. Wilson D, Roy D, Steyer G, Gargsha M, Stone M, McKinley E (2008) Whole mouse cryo-imaging. *Proc Soc Photo Opt Instrum Eng* 6916:69161I–69161I9
14. Burden-Gulley SM, Gates TJ, Burgoyne AM, Cutter JL, Lodowski DT, Robinson S, Sloan AE, Miller RH, Babilion JP, Brady-Kalnay SM (2010) A novel molecular diagnostic of glioblastomas: detection of an extracellular fragment of protein tyrosine phosphatase mu. *Neoplasia* 12:305–316
15. Zou KH, Warfield SK, Bharatha A, Tempany CM, Kaus MR, Haker SJ, Wells WM III, Jolesz FA, Kikinis R (2004) Statistical validation of image segmentation quality based on a spatial overlap index. *Acad Radiol* 11:178–189
16. Mendonca AM, Campilho A (2006) Segmentation of retinal blood vessels by combining the detection of centerlines and morphological reconstruction. *IEEE Trans Med Imaging* 25:1200–1213
17. Ma WY, Manjunath BS (2000) EdgeFlow: a technique for boundary detection and image segmentation. *IEEE Trans Image Process* 9:1375–1388
18. Johnson DH, Narayan S, Flask CA, Wilson DL (2010) Improved fat-water reconstruction algorithm with graphics hardware acceleration. *J Magn Reson Imaging* 31:457–465